Journal of Computational Physics 228 (2009) 3869–3881

Contents lists available at ScienceDirect

Journal of Computational Physics

journal homepage: www.elsevier.com/locate/jcp

A monolithic FEM-multigrid solver for non-isothermal incompressible flow on general meshes ☆

H. Damanik [a,*], J. Hron [b], A. Ouazzi [a], S. Turek [a]

[a] Institute of Applied Mathematics, TU Dortmund, Germany
[b] Institute of Mathematics, Charles University, Czech Republic

ARTICLE INFO

Article history:
Received 26 September 2008
Received in revised form 4 February 2009
Accepted 12 February 2009
Available online 1 March 2009

Keywords:
Monolithic multigrid
FEM
Non-isothermal
Incompressible flow

ABSTRACT

We present special numerical simulation methods for non-isothermal incompressible viscous fluids which are based on LBB-stable FEM discretization techniques together with monolithic multigrid solvers. For time discretization, we apply the fully implicit Crank–Nicolson scheme of 2nd order accuracy while we utilize the high order Q_2P_1 finite element pair for discretization in space which can be applied on general meshes together with local grid refinement strategies including hanging nodes. To treat the nonlinearities in each time step as well as for direct steady approaches, the resulting discrete systems are solved via a Newton method based on divided differences to calculate explicitly the Jacobian matrices. In each nonlinear step, the coupled linear subproblems are solved simultaneously for all quantities by means of a monolithic multigrid method with local multilevel pressure Schur complement smoothers of Vanka type. For validation and evaluation of the presented methodology, we perform the MIT benchmark 2001 [M.A. Christon, P.M. Gresho, S.B. Sutton, Computational predictability of natural convection flows in enclosures, in: First MIT Conference on Computational Fluid and Solid Mechanics, vol. 40, Elsevier, 2001, pp. 1465–1468] of natural convection flow in enclosures to compare our results with respect to accuracy and efficiency. Additionally, we simulate problems with temperature and shear dependent viscosity and analyze the effect of an additional dissipation term inside the energy equation. Moreover, we discuss how these FEM-multigrid techniques can be extended to monolithic approaches for viscoelastic flow problems.

1. Introduction

The underlying 'basic' flow model in this paper is governed by the Navier–Stokes equations which arise from the classical equations of continuity

$$\nabla \cdot \mathbf{u} = 0 \tag{1}$$

and the equations of motion with a body force term which is written as Boussinesq approximation

$$\rho \frac{\partial \mathbf{u}}{\partial t} + \rho \mathbf{u} \cdot \nabla \mathbf{u} = \nabla \cdot \mathbf{T} + \rho(1 - \gamma\Theta)\mathbf{j}, \tag{2}$$

☆ This research was supported by the Graduate School of Production Engineering and Logistics and by the German Research Foundation (DFG) through the collaborative research center SFB/TR TRR 30 and through the grants TU 102/11-3 (FOR493) and TU 102/21-1.

* Corresponding author.
E-mail addresses: hdamanik@math.tu-dortmund.de (H. Damanik), hron@karlin.mff.cuni.cz (J. Hron), ouazzi@math.tu-dortmund.de (A. Ouazzi), ture@featflow.de (S. Turek).

0021-9991/$ - see front matter © 2009 Elsevier Inc. All rights reserved.
doi:10.1016/j.jcp.2009.02.024

where $\mathbf{T} = -pI + 2\eta\mathbf{D}$ describes the constitutive material law; here, η may depend on the shear rate as well as on the temperature. Consequently, the Navier–Stokes equations are coupled with an energy equation to include the effect of temperature

$$\frac{\partial \Theta}{\partial t} + \mathbf{u} \cdot \nabla \Theta = \frac{1}{\sqrt{Ra\,Pr}} \nabla^2 \Theta, \tag{3}$$

where $\mathbf{u}, \rho, \gamma, \mathbf{j}, p, \eta, \mathbf{D}, Pr, Ra, \Theta$ are the velocity, density, thermal expansion, gravity vector, pressure, viscosity, symmetric part of gradient velocity, Prandtl number, Rayleigh number and temperature (see [6] for details). Moreover, we might also allow additional viscous dissipation terms in the energy equation which lead to more complex couplings.

Such non-isothermal nonlinear flow is very important in numerous applications since it is the basis of many complex flow problems with viscoelastic and multiphase fluids. Air flow inside a combustion engine or polymer flow in an injection molding or fluid flow in a heat exchanger are only few examples of viscous fluids where temperature is an important unknown. It becomes even more important when the fluid viscosity is temperature dependent: in this case, the temperature will indirectly give impact onto the velocity field through the viscosity, as we shall examine in Section 4.

One of the main issues for such simulations, besides the robustness and efficiency, is a reliable accuracy of the numerical solution. That leads us to utilize the LBB-stable conforming finite element pair Q_2P_1 which in our opinion belongs to the best finite element pairs regarding accuracy and robustness (see [1,14], the contributions according to [14] and in the proceeding [2]) for highly viscous incompressible flow, particularly together with local grid refinement techniques via hanging nodes. To preserve the high accuracy and robustness in nonstationary flow simulations, we apply implicit 2nd order time-stepping methods, for instance the Crank–Nicolson or Fractional-Step-θ scheme, which allow adaptive time stepping due to accuracy reasons only (see [25,28] for the corresponding details), but which do not depend on CFL-like restrictions.

However, the 'price' to be paid for the enhanced accuracy and robustness properties of such fully coupled approaches is the more expensive solution of the resulting coupled nonlinear discrete systems, either in each time step or in a direct stationary approach. While operator-splitting schemes, for instance classical projection or pressure correction methods, reduce the complete solution to a sequence of much easier scalar problems, the outer coupling of such subproblems towards the fully coupled solution is still a challenging problem, particularly if the energy equation has to be taken into account or in the case of shear, resp., temperature-dependent viscosities. The key problem in such approaches is the construction of optimal pressure Schur complement operators for updating the pressure which is even for the isothermal Navier–Stokes equations a challenge (see [16] for an overview). As an alternative, fully monolithic solvers have proven to be competitive, as demonstrated in [18,21,23] for non-isothermal problems as well as in [14,29,30] for fluid-structure interaction problems. Here, a Newton-like method is applied as outer iteration, which approximates the Jacobian matrices analytically or in a Black Box-like manner via divided differences, while the resulting linear systems are usually treated via Krylov space methods (see [7,15,19]). However, such Krylov space methods, like for instance BiCGStab or GMRES even with highly sophisticated preconditioners, typically suffer from convergence problems since the numerical behaviour strongly depends on the mesh size. In contrast, we discuss special monolithic multigrid solvers which exploit the underlying hierarchical mesh structures such that a mesh-independent and (almost) parameter-independent convergence behaviour can be obtained.

This paper is structured as follows: In the following Section 2, we discretize the flow problem in two space dimensions by utilizing the Q_2P_1 finite element pair in a standard FEM approach, after applying a standard implicit one-step time-stepping scheme in the nonstationary case. In Section 3, we treat the resulting discrete problems in a fully coupled monolithic way for $(\mathbf{u}, \Theta, p)$ by utilizing outer Newton iterations and inner multigrid solvers with special smoothers such that we maintain high efficiency and robustness, even on general meshes allowing the use of hanging nodes. In the numerical Section 4, we first consider natural convection flow in enclosures from the well-known MIT benchmark 2001 [5] to analyze the accuracy and efficiency of our new techniques for non-isothermal flow. This problem is well suited from the numerical point a view due to its simple geometry while at the same time complex phenomena in space and time arise. Moreover, this benchmark provides a large set of data for different approaches and methods to compare. Additionally, we demonstrate the numerical properties of the described methodology for non-isothermal flow with temperature and shear-rate dependent viscosity, and examine the numerical behaviour for additional viscous dissipation terms in the energy equation. Finally, we shortly discuss the natural extension of this monolithic approach for more complex nonlinear flow problems, particularly for viscoelastic fluids which require the coupling of the Navier–Stokes equations with tensor-valued differential equations for the extra stress.

2. Spatial and time discretization

2.1. Implicit time stepping

In the case of a standard one-step method, we need to solve for velocity, temperature and pressure at the current time step, $n+1$, with known values only from the previous time step, n. Then, as usual [25], the Navier–Stokes equations are discretized in time as follows

$$\begin{aligned}\frac{\mathbf{u}^{n+1} - \mathbf{u}^n}{\Delta t} &+ \theta\left[\mathbf{u}^{n+1} \cdot \nabla \mathbf{u}^{n+1} - (1 - \gamma\Theta^{n+1})\mathbf{j} - \frac{1}{\rho}(2\nabla \cdot \eta\mathbf{D}(\mathbf{u}^{n+1}))\right] + \frac{1}{\rho}\nabla p^{n+1} \\ &+ (1-\theta)\left[\mathbf{u}^n \cdot \nabla \mathbf{u}^n - (1 - \gamma\Theta^n)\mathbf{j} - \frac{1}{\rho}(2\nabla \cdot \eta\mathbf{D}(\mathbf{u}^n))\right] = 0,\end{aligned} \tag{4}$$

$$\nabla \cdot \mathbf{u}^{n+1} = 0, \tag{5}$$

where $\mathbf{u}^n \sim \mathbf{u}(t_n)$. The energy equation is discretized in the same way so that

$$\frac{\Theta^{n+1} - \Theta^n}{\Delta t} + \theta\left[\mathbf{u}^{n+1} \cdot \nabla\Theta^{n+1} - \frac{1}{\sqrt{RaPr}}\Delta\Theta^{n+1}\right] + (1-\theta)\left[\mathbf{u}^n \cdot \nabla\Theta^n - \frac{1}{\sqrt{RaPr}}\Delta\Theta^n\right] = 0. \tag{6}$$

By choosing, for instance, $\theta = \frac{1}{2}$, we obtain the fully implicit Crank–Nicolson method with second order accuracy which will be used in the following.

2.2. The conforming Stokes element Q_2P_1

After discretizing the system in time by the Crank–Nicolson scheme, leading to Eqs. (4)–(6), we discretize them in space by the finite element method using the Q_2P_1 element pair in two dimension. By Q_2P_1 we mean the standard biquadratic space with nine local degrees of freedom for each velocity/temperature component and three degrees of freedom for a piecewise linear discontinuous pressure approximation in each element. In 2D, there are in total 30 degrees of freedoms in each element consisting of velocity, temperature and pressure variables (see Fig. 1).

In order to reduce the global degrees of freedom, we also allow to apply local grid refinement techniques by using hanging nodes in a proper way where the values at hanging nodes must satisfy the continuity constraint of the neighboring nodes so that the finite element function remains globally continuous and hence conforming (see [3,17,32]). The refinement is done a priori, i.e. without any error indicator.

As usual we define the finite dimensional spaces W_h for temperature, V_h for velocity and L_h for the pressure approximations as

$$W_h := \left\{w_h \in H_0^1(\Omega_h) |\ w_{h|T} \in Q_2(T)\ \forall T \in T_h, \quad w_h = 0 \text{ on } \partial\Omega_h\right\}, \tag{7}$$

$$V_h := W_h \times W_h, \quad \text{and} \tag{8}$$

$$L_h := \left\{l_h \in L^2(\Omega_h) |\ l_{h|T} \in P_1(T)\ \forall T \in T_h\right\}, \tag{9}$$

and consider for each $T \in T_h$ the standard bilinear transformation $\psi_T : \widehat{T} \to T$ from the reference element $\widehat{T}$ to the unit square T. Then, $Q_2(T)$ is defined as

$$Q_2(T) := \left\{q \circ \psi_T^{-1} | q \in \text{span}\langle 1, x, y, xy, x^2, y^2, x^2y, y^2x, x^2y^2\rangle\right\} \tag{10}$$

with local degrees of freedom located at the vertices, at the midpoints of the edges and in the center of the quadrilateral T. The space $P_1(T)$ consists of linear functions defined by

$$P_1(T) = \left\{q \circ \psi_T^{-1} : q \in \text{span}\langle 1, x, y\rangle\right\} \tag{11}$$

with the function values and both partial derivatives located in the center of each quadrilateral T, leading to three local degrees of freedom which gives a discontinuous pressure.

Regarding stability and accuracy properties of this element pair, the inf–sup condition is satisfied (see [4]); however, the combination of the bilinear transformation ψ_T with a linear function on the reference square would imply that the basis on the reference square does not contain the full bilinear basis. So, the method can be only first order accurate on general meshes (see [1,4])

$$\|p - p_h\|_0 = O(h). \tag{12}$$

The standard remedy is to consider a local coordinate system (ξ, η) obtained by joining the midpoints of the opposing faces of T (see [1,20,27]). Then, we set on each element T

$$P_1(T) := \text{span}\langle 1, \xi, \eta\rangle. \tag{13}$$

For this case, the inf–sup condition is also satisfied and the second order approximation is recovered for the pressure as well as for the velocity gradient (see [4,12])

$$\|p - p_h\|_0 = O(h^2) \quad \text{and} \quad \|\nabla u - \nabla u_h\|_0 = O(h^2). \tag{14}$$

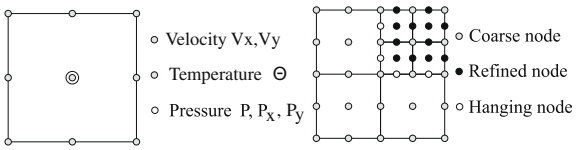

Fig. 1. Left: Local degrees of freedom for Q_2P_1. Right: Locally refined element.

For a smooth solution, the approximation error for the velocity in the L_2-norm is of order $O(h^3)$ which can be easily demonstrated for prescribed polynomials or for smooth data on appropriate domains.

Finally, by rearranging the discretized equations (4)–(6) into algebraic systems, we end up with the following compact form of nonlinear system of equations in each time step

$$\begin{cases} S_{\mathbf{u}}(\mathbf{u}^{n+1})\mathbf{u}^{n+1} + \mathbf{j}M_\Theta \Theta^{n+1} + Bp^{n+1} = f(n+1,n), \\ S_\Theta(\mathbf{u}^{n+1})\Theta^{n+1} = g(n+1,n), \\ B^T\mathbf{u}^{n+1} = 0 \end{cases} \tag{15}$$

with S describing the reactive, diffusive, and convective terms from the governing equations above, and $\mathbf{u} = (u, v)$ consisting of components u and v, while M and B describing the mass matrix and gradient matrix.

3. Iterative solvers

Applying the standard finite element method with the Q_2P_1 element pair as described above, this approach leads to nonlinear systems of equations as indicated in (15). Each nonlinear system is then solved by a Newton iteration which has a well-known quadratic convergence if the initial solution is chosen close enough to the exact solution (see [15,19,26] which shows the excellent convergence rates of Newton iteration in comparison with fixed point methods for non-isothermal flow).

The basic idea of the Newton iteration is to find a root of a function, $\mathbf{R}(\mathbf{X}) = \mathbf{0}$, using the available known function value and its first derivative,

$$\mathbf{X}^{l+1} = \mathbf{X}^l + \omega^l \mathbf{j}^{-1}(\mathbf{X}^l)\mathbf{R}(\mathbf{X}^l) \tag{16}$$

with $\mathbf{X} = (u_h, v_h, \Theta_h, p_h)$ in our setting and $\mathbf{j}(\mathbf{X}^l) = \left[\frac{\partial \mathbf{R}(\mathbf{X}^l)}{\partial \mathbf{X}}\right]$ is the Jacobian matrix. Here, $\mathbf{R}(\mathbf{X}^l) = \begin{pmatrix} \mathrm{def}_u^l & \mathrm{def}_v^l & \mathrm{def}_\Theta^l & \mathrm{def}_p^l \end{pmatrix}^T$ is the residual coming from the discrete problem of the system (15) and ω^l is some damping parameter which has to be determined such that certain error measures decrease (see [11] and for implementation see also [14,27]). In the next step we will discuss how to deal with the Jacobian before we discuss how to solve the linear subproblems in each nonlinear step. In our approach, we approximate the first derivative (the Jacobian) using divided differences

$$\left[\frac{\partial \mathbf{R}(\mathbf{X}^l)}{\partial \mathbf{X}}\right]_{ij} \approx \frac{\mathbf{R}_i(\mathbf{X}^l + \epsilon e_j) - \mathbf{R}_i(\mathbf{X}^l - \epsilon e_j)}{2\epsilon}, \tag{17}$$

where $e_j = \delta_{ij}$ is the standard Kronecker symbol. Another possibility is to calculate the Frechét derivative at the continuous level, which however can be very complicated for complex nonlinear flow models (see [26,27]).

For small system (i.e. less than 20.000 unknowns) a direct linear solver like UMFPACK is often preferable. But for large system, its memory requirement is far too high. Therefore, we choose as an alternative a multigrid method which is today one of the fastest iterative linear solvers for CFD problems (see [33]). Inside multigrid, a restriction operator is applied to the residual after pre-smoothing on the actual mesh level and a direct linear solver is utilized to obtain the coarsest grid solution. Prolongation is then applied which is followed by post-smoothing to give a better approximation. These steps continue until a V or F-cycle of multigrid iterations is finished. We use a fixed number of smoothing steps of a special 'Vanka' smoother which acts locally in each element Ω_i on all levels and which can be written as

$$\begin{pmatrix} u^{k+1} \\ v^{k+1} \\ \Theta^{k+1} \\ p^{k+1} \end{pmatrix} = \begin{pmatrix} u^{k} \\ v^{k} \\ \Theta^{k} \\ p^{k} \end{pmatrix} - \omega^k \sum_{\Omega_i} \begin{pmatrix} S_{uu}|_{\Omega_i} & S_{uv}|_{\Omega_i} & j_1 M|_{\Omega_i} & B_u|_{\Omega_i} \\ S_{vu}|_{\Omega_i} & S_{vv}|_{\Omega_i} & j_2 M|_{\Omega_i} & B_v|_{\Omega_i} \\ S_{\Theta u}|_{\Omega_i} & S_{\Theta v}|_{\Omega_i} & S_\Theta|_{\Omega_i} & 0 \\ B_u^T|_{\Omega_i} & B_v^T|_{\Omega_i} & 0 & 0 \end{pmatrix}^{-1} \mathbf{R}(\mathbf{X}^k) \tag{18}$$

with $\mathbf{R}(\mathbf{X}^k) = \begin{pmatrix} \mathrm{def}_u^k & \mathrm{def}_v^k & \mathrm{def}_\Theta^k & \mathrm{def}_p^k \end{pmatrix}^T$ (see [27,31,8] for more details).

Here, the 'summation' over each element represents an assembling technique. The above iteration is adapted to the linearization of Eq. (15) where the additional nonzero blocks inside the Jacobian arise from the dependency on the vector of unknowns of the nonzero blocks in Eq. (15). For example, in the temperature equation of Eq. (15), the S operator depends on the velocity vector, too. Hence, there will be nonzero blocks in the velocity column of the temperature row of the Jacobian. In this way, one can see which block will be nonzero in the local system. Then, the inverse of the local systems on each element Ω_i (of size 30×30) is computed by a direct linear solver.

4. Numerical analysis

In this section we will present numerical results of benchmarking type for several problem settings. The first is the MIT Benchmark 2001 [5] where we demonstrate that our non-isothermal code can reproduce the benchmark results. Then, we perform numerical simulations for a problem with temperature and shear dependent viscosity. Finally, we add a dissipation

term into the energy equation in order to have the effect of viscous heating along the fluid flow and perform corresponding numerical simulations.

4.1. MIT Benchmark 2001

The MIT Benchmark 2001 [5] describes heat driven cavity flow in a 8:1 rectangular domain at near-critical Rayleigh number. Why near-critical? Because the onset of thermal convection will occur at the critical number, beyond that non-periodical up to turbulent flow is resulting.

The geometry of the problem is very simple (see Fig. 2) but leads nevertheless to complex multiscale phenomena. The velocity vector at the upper and bottom wall is zero which describes a non-slip condition. The left wall is heated while the right wall is cooled by a prescribed non-dimensional temperature of -0.5 and 0.5. Gravity is applied downwards. The top and bottom of the walls are insulated, which means that homogeneous Neumann boundary conditions for the temperature are set and hence no heat is going outside of the wall. The initial condition is the zero vector for all variables. Physically relevant variables which are to be computed are the velocity and temperature at point 1, and the Nusselt number along both sides of the wall. The time step is chosen so that there are enough data points in one oscillation of the resulting variables to graphically postprocess all quantities and so that smaller time steps do not significantly improve the solutions with respect to quantitative measurements. After comparison with the results from Davis [10], Gresho [13], Turek [26] and Le Quéré [24] we choose approximately 34 time steps in one oscillation which corresponds to $\Delta T = 0.1$ as time step size.

Several meshes have been used to perform the spatial discretization (see Table 1). The coarse mesh has approximately 1:5 x-to-y ratio of grid points and decreases gradually towards the walls (see Fig. 3).

This figure also describes how the local refinement is generated for some exemplary meshes. We set the local refinement to be at both sides of the wall. This judgment is subject to the Nusselt number which is of interest for the engineer,

$$Nu(t) = \frac{1}{H}\int_0^H \left|\frac{\partial \Theta}{\partial x}\right|_{x=0,W} dx, \tag{19}$$

where H and W are the height and the width of the domain. The meshes are denoted by 'nR_ai' for i local refinement steps after n regular refinements. However, we have to explicitly state that the level of grid refinement towards the walls has not been chosen on the basis of an a posteriori error indicator, but a priori only, since it was the primary aim of these studies to show that local alignment together with hanging nodes can be directly integrated into this monolithic approach without any loss of efficiency while gaining higher accuracy. The combination with user-defined a posteriori error control mechanisms which lead to an automatic grid refinement, resp., grid coarsening is part of future studies with this full Galerkin approach.

The level 2 mesh (2R, meaning '2 times regular refinement' of the coarse mesh) is used to perform the first computation until the solution reaches a periodical result (after 1500 non-dimensional time units), then the last output result is used as a

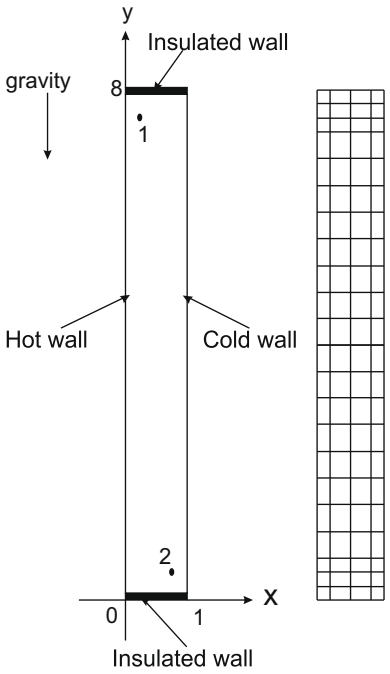

Fig. 2. Geometry and coarse mesh.

Table 1
Contributor's and our testing meshes.

Author	Turek	Davis	Gresho	Le Quéré
Mesh	128×704	83×403	105×481	48×180
Mesh	Elements	Nodes	Edges	Dof
2R	1408	1513	2920	21,747
2R_a1	1936	2043	3978	29,679
2R_a5	17,776	17,891	35,666	267,327
3R	5632	5841	11,472	85,731
3R_a1	6688	6899	13,586	101,583
3R_a4	21,472	21,689	43,160	323,379
4R	22,528	22,945	45,472	340,419
4R_a1	24,640	25,059	49,698	372,111
4R_a3	37,312	37,735	75,046	562,215

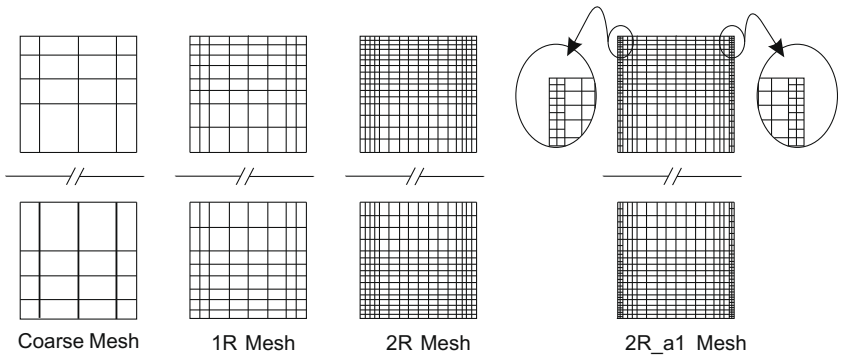

Fig. 3. Several hierarchies and types of meshes.

starting point for the following computation. Note that regular refinement doubles the number of elements in both x- and y-direction. The results of the MIT Benchmark 2001 configuration computed by our new approach oscillate periodically in time (see Fig. 4) and are presented in Table 2.

Several comparisons have been made to see the difference from the other references. In [13] it is mentioned that the Q_2P_1 element with coarse mesh (27×121) performs poorly in the sense that the results show too low amplitudes for velocity and temperature at point 1 (0.00542 and 0.00442). In contrast, we observe good results even with the level 2 mesh (16×88). They also calculated Nusselt numbers which are slightly different from the reference, see [24]. In fact, we produce the same results (2R,3R,4R), but only as soon as we introduce local refinement near the wall, the Nusselt number improves strongly even with the level 2 mesh. It is obvious that the Nusselt number calculated on levels 3 and 4 (3R and 4R) can be improved by using the level 2 mesh with local refinement (2R_a1 and 2R_a5).

We believe that without local grid refinement we might have to use level 5 or higher to produce nearly the same Nusselt numbers as the one produced by Le Quéré. This information shows us the expected result that local grid refinement helps a lot for this test configuration. The time step is not an issue as long as we put enough time steps over one period. Twenty up to fourty time steps are already sufficient to produce excellent results for this problem, and no specific gain/loss in the quality of the Nusselt number has been observed if we increase/decrease the number of time steps in one period (see [8]). Summa-

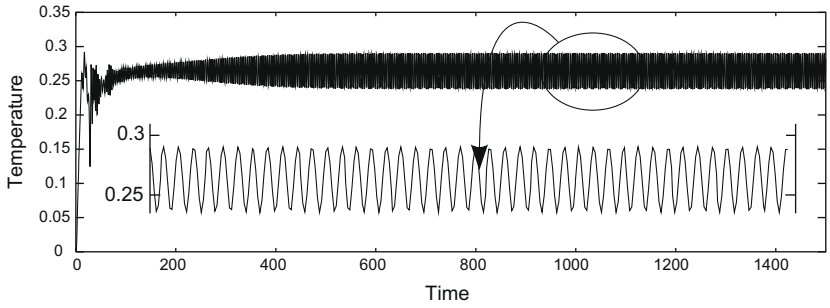

Fig. 4. Temperature oscillations at point 1.

Table 2
Results of the MIT benchmark 2001 simulations.

Author	u_1	Θ_1	−Nu	Period
Turek	0.0572	0.2647	4.5791	3.422
Davis	0.0563	0.2655	4.5796	3.412
Gresho	0.05665	0.26547	4.5825	3.4259
Le Quéré	0.056356	0.26548	4.57946	3.4115
2R	0.058139	0.26539	4.66245	3.4000
2R_a1	0.057674	0.26538	4.59295	3.4214
2R_a5	0.057490	0.26540	4.57941	3.4214
3R	0.056787	0.26548	4.59318	3.4214
3R_a1	0.056665	0.26546	4.58155	3.4214
3R_a4	0.056591	0.26549	4.57967	3.4214
4R	0.056451	0.26549	4.58158	3.4200
4R_a1	0.056394	0.26546	4.57994	3.4154
4R_a3	0.056372	0.26546	4.57969	3.4214

Table 3
Mesh information for channel problem.

Mesh	Elements	Nodes	Edges	Dof
1R	752	1095	1846	13,335
1R_a1	2264	2849	5112	37,467
1R_a2	5264	5847	11,110	82,455
2R	3008	3693	6700	49,227
2R_a1	6008	6691	12,698	94,215
3R	12,032	13,401	25,432	188,691

rizing, we observe differences from the reference result with 0.02% for velocity u_1 and with 0.003% for temperature Θ_1; and we are very close with 0.004% difference for the Nusselt number.

4.2. Temperature-dependent viscosity in a heat exchanger

After validating the proposed monolithic approach for this standard MIT Benchmark 2001, we proceed with more complex non-isothermal problems to demonstrate the flexibility and efficiency for such configurations. As a first example, we consider flow with temperature-dependent viscosity through small channels which is a very common shape of heat exchangers and which leads already to complex flow behavior. In order to study this behavior, a flow configuration is set in which different temperature values as Dirichlet boundary data at each of the channels is implemented. Qualitatively, it is expected that the flow will stop when the viscosity grows to a large value caused by temperature differences. Therefore, for prototypical test simulations the viscosity is prescribed through the relation

$$\eta = \eta_0 e^{\left(a_1 + \frac{a_2}{a_3 + \Theta}\right)} (b_1 + b_2 \|\mathbf{D}\|)^{-b_3}, \tag{20}$$

where a_1, a_2, a_3 and b_1, b_2, b_3 are specific material parameters, and $\|\mathbf{D}\| = \sqrt{D_{ij} D_{ij}}$ (see [8]] for more details).

Here, $\mathbf{D} = \frac{1}{2}(\nabla \mathbf{u} + \nabla \mathbf{u}^T)$ is the usual symmetric part of the gradient velocity. Fig. 5 gives an example for specific material parameters which however does not yet correspond to a certain type of fluid, because we do not investigate experimental data at the moment. Further examples with more general parameter settings, particularly with additional shear dependent behaviour, are examined in [9].

We consider the specific geometry (width = 3.5 and length = 44 in non-dimensional units) and setting given in Table 3 and Fig. 6 which shows four channels installed for low Reynolds number flow ($Re \approx 14$). The hot fluid enters the inflow section with non-dimensional temperature $\Theta = 250$ and with a parabolic profile of velocity, and the heat is then distributed to all channels. We specify Dirichlet data for the temperature ($\Theta = 190$) to all channels except to the second channel ($\Theta = 180$) to control the fluid flow at this pipe. This slightly different temperature will nevertheless increase the viscosity difference to 'stop' the flow at the corresponding channel. We present in Fig. 7 the resulting flow which almost stops at the second channel caused by a locally growing viscosity. In the left figure, we start with prescribing the same temperature ($\Theta = 190$) to all channels (the viscosity value is set to 0.001 at all channels) while in the right figure, we change the temperature at the second channel to $\Theta = 180$. Hence, viscosity at this channel grows to 0.0144 (≈ 14 times bigger than before), and finally the flow is 'stopped' at this channel.

On this geometry, we compute for mesh 1R, 2R, 3R, 1R_a1, 1R_a2 and 2R_a1 (see Fig. 8). The local refinement is set for channels 1, 3, and 4. All initial solutions start from zero. Table 4 shows how the proposed method converges with respect to a

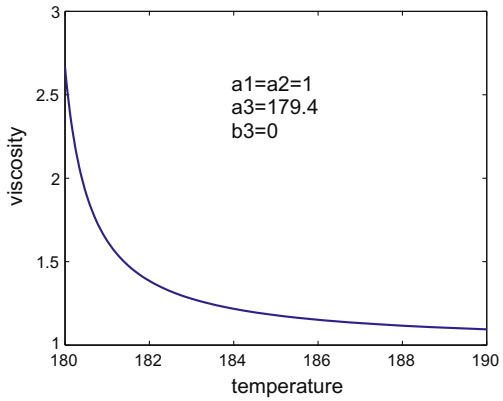

Fig. 5. Non-dimensional temperature-dependent viscosity with $a_1 = a_2 = 1.0, a_3 = 179.4, b_3 = 0, \eta_o = 1.0$.

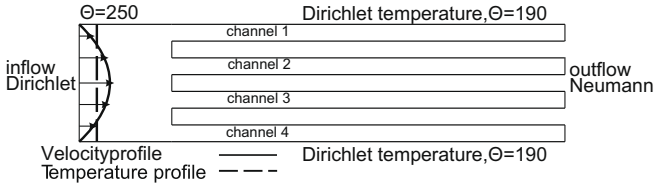

Fig. 6. Setup for the channel problem.

given number of digits for the linear multigrid solver. Here, #NL denotes the number of Newton iteration, while #MG presents the averaged number of multigrid iterations per nonlinear step. We can see from Table 4 that the local refinement does not disturb the multigrid convergence. The memory requirement of our computer is still capable to run a direct linear solver (UMFPACK) for this problem at least up to three refinements. In our case, we can force multigrid by decreasing the linear tolerance to get close to UMFPACK results with respect to the number of nonlinear iterations. It is clear that for linear tolerance of $TOL = 10^{-8}$ the computation needs more or less the same number of nonlinear iterations as with UMFPACK. For this

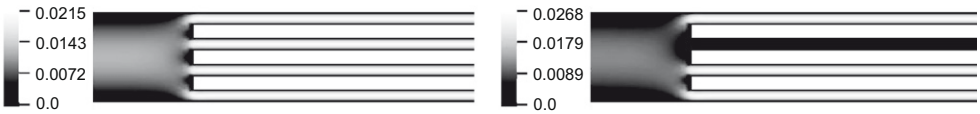

Fig. 7. The Euclidean norm of velocity. Left: The flow is not blocked. Right: The flow at the second channel is blocked.

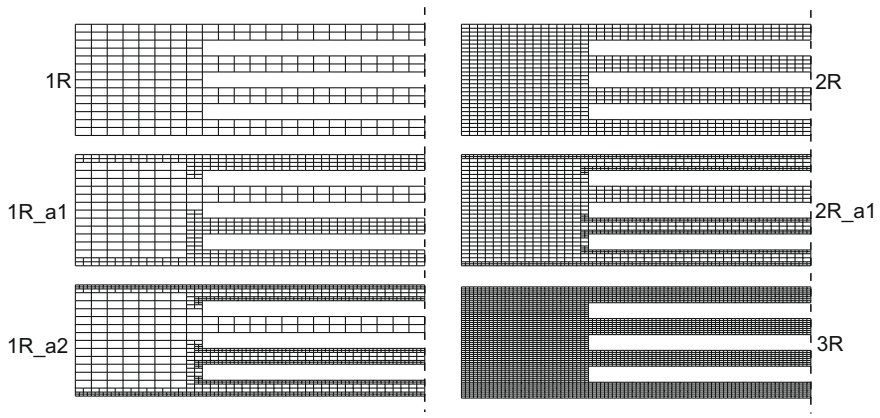

Fig. 8. All computed meshes.

Table 4
#NL/#MG for different levels, with Tol denoting the linear stopping criterion.

Tol/level	1R	2R	3R	1R_a1	1R_a2	2R_a1
10^{-1}	10/1	9/1	10/1	9/1	9/1	8/1
10^{-2}	7/1	7/2	7/2	7/1	7/1	7/2
10^{-3}	6/1	6/2	6/3	6/1	6/1	6/2
10^{-8}	5/5	5/6	5/8	5/4	5/4	5/5
UMFPACK	5/–	5/–	4/–	5/–	5/–	5/–

small problem, UMFPACK is (still) faster than our current multigrid implementation with respect to computation time. In the future, for large three dimensional problem, we plan to update our multigrid approach focusing on fast linear iterative solver.

In the following, we also test this principle on a more complex geometry which has more channels in it. This configuration is prototypically used in chemical micro-reactor processes. Fig. 9 shows typical flow profiles when we simulate the flow with constant viscosity ($a_1 = a_2 = b_3 = 0$), while in Fig. 10 we try to stop the flow of the fluid through all channels which lay in the middle of the geometry (white color) and allow the fluid to flow only through the top and bottom channels of the geometry (dark color), again by prescribing different wall temperature values as boundary condition. Both figures and Fig. 11 show clearly the different flow profiles with respect to the different parameters governing the viscosity. This leads to the idea of a 'non-mechanical valve' which can be controlled by setting the outside temperature only. As a prototypical application, one may think of hot pattex material (for glue purposes) which can flow when the temperature increases and which will become an elastic solid when the temperature decreases, thus stopping the flow.

4.3. Viscous dissipation term inside the energy equation

Finally, we analyze the effect of adding a viscous dissipation term into the equation of energy where at the moment the stress tensor is just the symmetric part of the velocity gradient (see Eq. (21)). The additional term has the physical meaning of producing viscous heat along with the fluid flow [22]. The heat which is generated from this friction may dramatically change the temperature and velocity profile of the flow which is of interest in the study of polymer flow. Hence, the new equation can be rewritten as

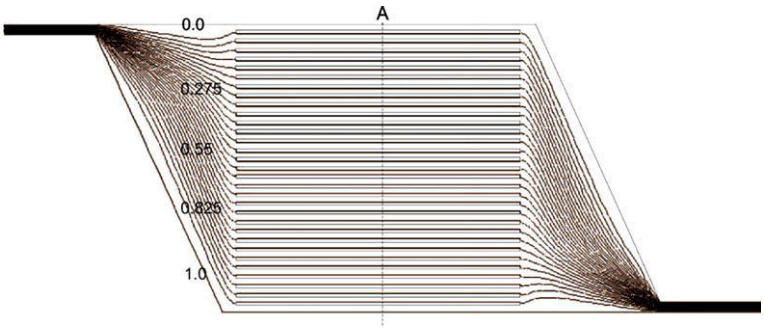

Fig. 9. Streamlines for flow with constant viscosity.

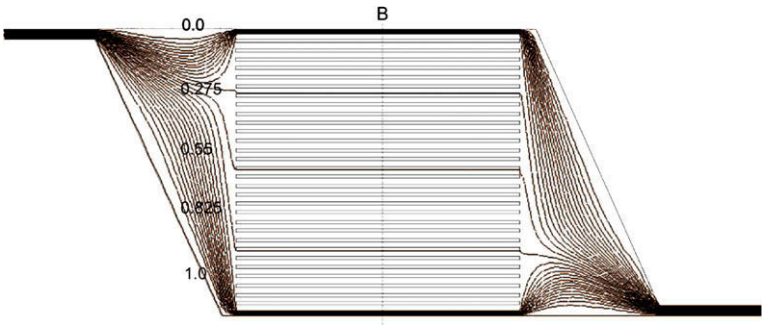

Fig. 10. Streamlines for the 'stopping' flow with different temperature boundary values.

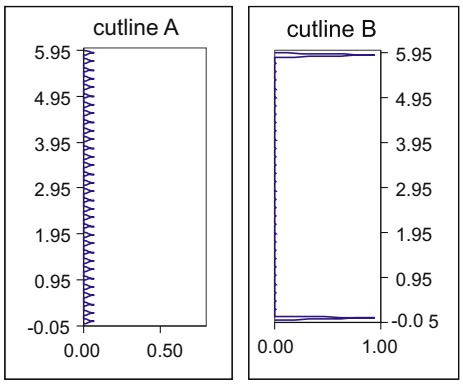

Fig. 11. Cutline A and B of the norm of velocity.

$$\frac{\partial \Theta}{\partial t} + \mathbf{u} \cdot \nabla \Theta = \mathbf{D} : \mathbf{D} + \nabla \cdot (k \nabla \Theta). \tag{21}$$

The new equation is comparable with Eq. (3) where $k \equiv 1/\sqrt{Ra\,Pr}$ but with an additional term which is defined by the scalar product of the symmetric part of the velocity gradient with itself. We test the modified model with constant viscosity ($\eta = \eta_0$) for the well-known 4 to 1 contraction geometry and apply a non-slip condition at the upper wall while prescribing the half of the parabolic velocity profile at the inflow due to its symmetry (see Fig. 12). By neglecting the time derivative, $\frac{\partial \Theta}{\partial t} = 0$, we directly calculate the stationary result with the proposed Newton-multigrid solver. Although we prescribe zero temperature at the inflow, along the channel heat is produced as the friction becomes higher. Generally, it gives additional heat locally as the material begins to flow. We refer to Fig. 13 to show qualitatively the effect of the additional term. One can see from the cutline diagram ($y = 0$) that near the inflow ($-20 < x < 0$) heat is produced slowly, but that after entering the contraction ($0 < x < 20$) there is a big gradient of temperature up to the end of the channel. The component of velocity and of the stress tensor also show that the computation may face numerical difficulties around the entrance. The characteristic of such a geometry appears clearly from the entrance point where the sharp corner point may cause numerical problems in viscoelastic flow since then the stress tensor will raise to a huge value (see Fig. 14). That is why we make local refinement around the entrance corner and also at the end of the channel to get a better capture of the temperature field. Table 5 shows how the Newton-Multigrid and Newton-UMFPACK solver converge for this kind of problem. It is clear that our proposed method seems to be robust with respect to using local refinement. As a test configuration, we use low inertia flow, $Re \sim 2.5$, which is as typically controlled by the velocity profile, characteristic length of the width of channel, and the given viscosity. The meshes as well as the isoline of axial stress tensor are shown in Fig. 15 which stresses again the role of adaptive refinement. Here, mesh $1R\_a1$ is comparable with mesh $2R$, and mesh $1R\_a2$ or mesh $2r\_a1$ are comparable with mesh $3R$. This situation is also illustrated in Fig. 16 where the axial stress profiles are compared along the entrance line ($x = 0$).

These prototypical studies have to be seen as preparing simulation for more complex flow configurations for which we will extend **T** to a model which adds the elastic part of a viscoelastic stress tensor $\boldsymbol{\sigma}^p$. The stress tensor will replace **D** to pro-

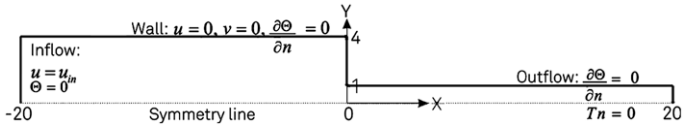

Fig. 12. Geometry of the 4 to 1 contraction configuration.

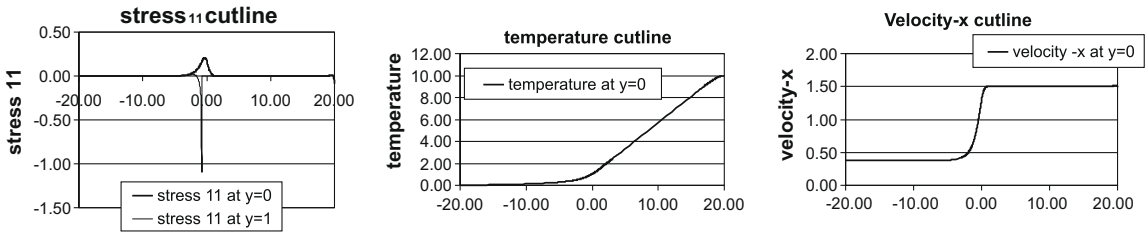

Fig. 13. The cutlines of $T_{11}, \theta,$ and u_x.

Table 5
#NL/#MG for different levels, with Tol denoting the linear stopping criterion.

Tol/level	1R	2R	3R	1R_a1	1R_a2	2R_a1
10^{-1}	11/1	12/2	12/2	13/1	12/1	11/1
10^{-2}	9/2	10/3	10/4	9/2	9/2	9/2
10^{-3}	9/4	9/5	9/6	9/2	9/3	9/3
10^{-8}	9/13	9/17	9/19	9/7	9/7	9/9
UMFPACK	9/–	9/–	9/–	9/–	9/–	9/–

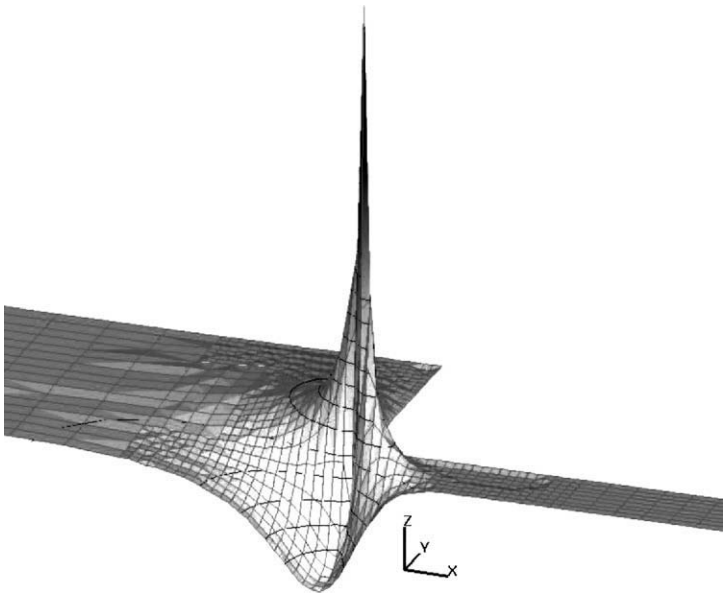

Fig. 14. 3D representation of stress tensor component for the 2*R_a*1 mesh.

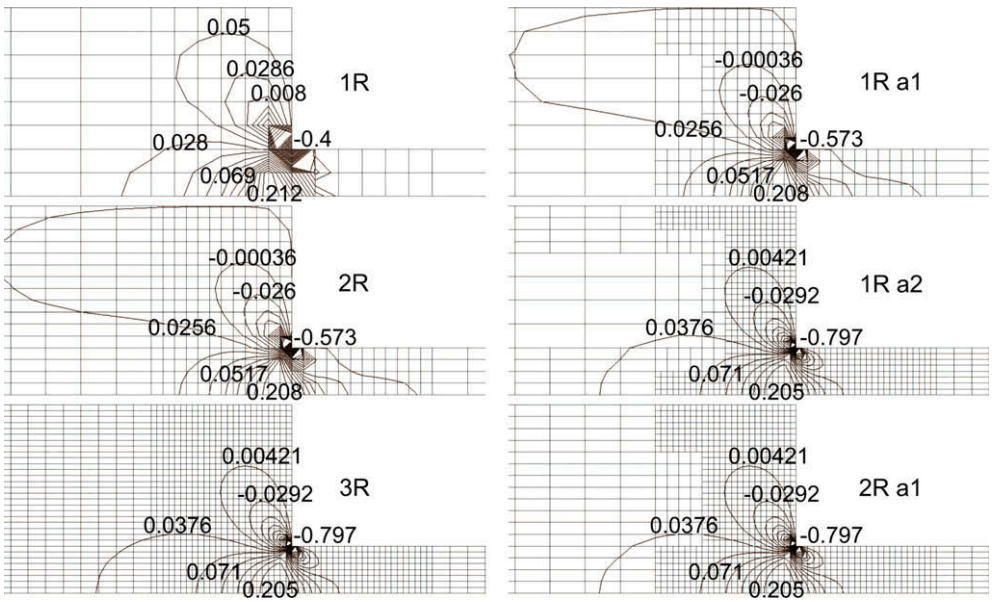

Fig. 15. Isolines for the stress tensor on several different meshes. Note the different scale between mesh 1R, 2R, and 3R.

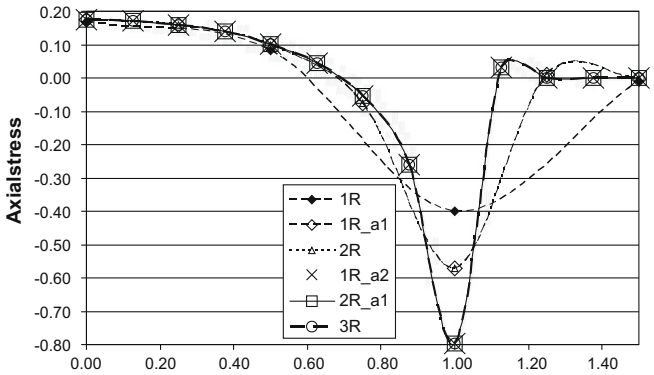

Fig. 16. Axial stress profile along the entrance line $x = 0$.

duce a better physical meaning of additional heat along the flow due to viscous dissipation. And since the stress tensor will raise at the entrance point of the geometry, the viscous dissipation term will be an interesting subject for the numerical tests (see [9]).

5. Conclusion

We have presented new FEM simulation techniques for non-isothermal viscous flow described by the Navier–Stokes equations and the Boussinesq approximation, hereby allowing temperature and shear dependent behaviour of the viscosity. The resulting discrete problems, after discretization in space and time, are solved via Newton iteration and special monolithic multigrid methods which are adapted to the utilized Q_2P_1 finite element pair. Numerical results for validation of the methodology are provided for the MIT Benchmark 2001 configuration which leads to periodically oscillating flow behaviour. Here, the high order FEM approach together with 2nd order fully implicit time stepping and local grid refinement leads to very accurate simulations for this dynamical configuration with many different flow scales. Additionally, we simulate two additional problems with prototypical temperature-dependent viscosity and with dissipation term inside the energy equation which can be seen as a first step towards viscoelastic flow. Exemplary results are shown to demonstrate the numerical behaviour of this fully implicit monolithic FEM-multigrid approach which can be extended to more complex flow problems in a quite straightforward way.

References

[1] D.N. Arnold, D. Boffi, R.S. Falk, Approximation by quadrilateral finite element, Mathematics of Computation 71 (239) (2002) 909–922.
[2] K.J. Bathe (Ed.), Proceedings of the First MIT Conference on Computational Fluid and Solid Mechanics, vol. 2, June 12–15, 2001.
[3] E. Bänsch, Local mesh refinement in 2 and 3 dimension, IMPACT of Computing in Science and Engineering 3 (1991) 181–191.
[4] D. Boffi, L. Gastaldi, On the Quadrilateral Q2-P1 Element for the Stokes Problem, International Journal for Numerical Methods in Fluids 39 (2002) 1001–1011.
[5] M.A. Christon, P.M. Gresho, S.B. Sutton, Computational predictability of natural convection flows in enclosures, First MIT Conference on Computational Fluid and Solid Mechanics, vol. 40, 2001, pp. 1465–1468.
[6] M.A. Christon, P.M. Gresho, S.B. Sutton, Computational predictability of natural convection flows in enclosures, International Journal for Numerical Methods in Fluids 40 (2002) 953–980.
[7] N.B. Cheikh, B.B. Beya, T. Lili, A multigrid method for solving the Navier–Stokes/Boussinesq equations, Communications in Numerical Methods in Engineering 24 (2008) 671–681.
[8] H. Damanik, Numerical simulation of highly viscous non-isothermal viscoelastic fluids, Ph.D. Thesis, TU Dortmund, Germany, 2009.
[9] H. Damanik, J. Hron, A. Ouazzi, S. Turek, A monolithic FEM approach for temperature and shear dependent viscosity in viscoelastic flow, 2009.
[10] D. Davis, E. Bänsch, An operator-splitting finite-element approach to the 8:1 thermal cavity problem, International Journal for Numerical Methods in Fluids 40 (2002) 1019–1030.
[11] J.E. Dennis Jr., R.B. Schnabel, Numerical Methods for Unconstrained Optimization and Nonlinear Equations, SIAM, 1996.
[12] P.M. Gresho, On the theory of semi-implicit projection methods for viscous incompressible flow and its implementation via a finite element method that also introduces a nearly consistent mass matrix, Part 1: Theory, International Journal for Numerical Methods in Fluids 11 (1990) 587–620.
[13] P.M. Gresho, S.B. Sutton, Application of the FIDAP code to the 8:1 thermal cavity problem, International Journal for Numerical Methods in Fluids 40 (2002) 1083–1092.
[14] J. Hron, S. Turek, A monolithic FEM/Multigrid Solver for ALE formulation of fluid structure interaction with application in biomechanics, in: H.-J. Bungartz, M. Schäfer (Eds.), Fluid-Structure Interaction – Modelling, Simulation, Optimization, Lecture Notes in Computational Science and Engineering, vol. 53, Springer, 2006, ISBN 3-540-34595-7, pp. 146–170.
[15] D.A. Knoll, V.A. Mousseau, On Newton–Krylov Multigrid Methods for the Incompressible Navier–Stokes equations, Journal of Computational Physics 163 (2000) 262–267.
[16] D. Kuzmin, R. Lhner, S. Turek (Eds.), Flux-Corrected Transport: Principles, Algorithms, and Applications, Springer Scientific Computation, 2005.
[17] A. Meyer, Projected PCGM for handling hanging nodes in adaptive finite element procedures, Preprint SFB393/99-25, TU Chemnitz, 1999.
[18] P.R. McHugh, D.A. Knoll, Fully coupled finite volume solutions of the incompressible Navier–Stokes and energy equations using an inexact Newton method, International Journal for Numerical Methods in Fluids 19 (1994) 439–455.
[19] M. Pernice, M.D. Tocci, A multigrid-preconditioned Newton–Krylov method for the incompressible Navier–Stokes equations, SIAM Journal on Scientific Computing 23 (2) (2001) 398–418.

[20] R. Rannacher, S. Turek, A simple nonconforming quadrilateral Stokes element, Numerical Methods for Partial Differential Equations 8 (1992) 97–111.
[21] A.G. Salinger, R.B. Lehoucq, R.P. Pawlowski, J.N. Shadid, Computational bifurcation and stability studies of the 8×1 thermal cavity problem, International Journal for Numerical Methods in Fluids 40 (8) (2002) 1059–1073.
[22] W.R. Schowalter, Mechanics of Non-Newtonian Fluids, Pergamon Press, 1978.
[23] J.N. Shadid, A.G. Salinger, R.P. Pawlowski, P.T. Lin, G.L. Hennigan, R.S. Tuminaro, R.B. Lehoucq, Large-scale stabilized FE computational analysis of nonlinear steady-state transport/reaction systems, Computer Methods in Applied Mechanics and Engineering 195 (2006) 1846–1871.
[24] Shihe Xin, P. Le Quéré, An extended Chebyshev pseudo-spectral benchmark for the 8:1 differentially heated cavity, International Journal for Numerical Methods in Fluids 40 (2002) 981–998.
[25] S. Turek, A comparative study of time-stepping techniques for the incompressible Navier–Stoke equations: from fully implicit non-linear schemes to semi-implicit projection methods, International Journal for Numerical Methods in Fluids 22 (1996) 987–1011.
[26] S. Turek, R. Schmachtel, Fully coupled and operator-splitting approaches for natural convection flows in enclosures, International Journal for Numerical Methods in Fluids 40 (2002) 1109–1119.
[27] S. Turek, Efficient Solvers for Incompressible Flow Problems: An Algorithmic and Computational Approach, LNCSE, vol. 6, Springer-Verlag, 1999.
[28] S. Turek, L. Rivkind, J. Hron, R. Glowinski, Numerical study of a modified time-steeping theta-scheme for incompressible flow simulations, Journal of Scientific Computing 28 (2–3) (2006) 533–547.
[29] S. Turek, J. Hron, A monolithic FEM solver for an ALE formulation of fluid-structure interaction with configuration for numerical benchmarking, in: P. Wesseling, E. Onate, J. Periaux (Eds.), Books of Abstracts European Conference on Computational Fluid Dynamics, vol. 176, Eccomas CFD 2006, 2006.
[30] S. Turek, J. Hron, Numerical techniques for multiphase flow with liquid–solid interaction, in: G.P. Galdi, R. Rannacher, A.M. Robertson, S. Turek (Eds.), Hemodynamical Flow Modeling, Analysis and Simulation, Oberwolfach Seminars, vol. 37, Birkhäuser, 2008, pp. 379–501.
[31] S. Turek, A. Ouazzi, J. Hron, A computational comparison of two FEM solvers for nonlinear incompressible flow, in: Challenges in Scientific Computing CISC 2002, LNCSE, Springer, 2002, pp. 87–109.
[32] R. Verfürth, A Review of a Posteriori Error Estimation and Adaptive Mesh Refinement Techniques, Wiley and Teubner, Chichester and Stuttgart, 1996.
[33] P. Wesseling, An Introduction to Multigrid Methods, John Wiley & Sons, 1992.